Progress on Quantitative Infrared Thermography at the NASA Langley Aerothermodynamic Laboratory

F. Drew Turbeville*, Casey J. Broslawski†, Jonathan S. Cheatwood‡
NASA Langley Research Center, Hampton, VA, 23681, USA

A quantitative infrared thermography technique is being developed for accurate and high-resolution measurements of surface temperature and heat flux in the hypersonic wind tunnels at NASA Langley Research Center. A hemisphere test campaign was carried out in the Langley Aerothermodynamic Laboratory 20-Inch Mach 6 Air Tunnel to assess the current performance of the technique and to identify remaining challenges. Measurements were obtained for three different model materials over a range of freestream Reynolds numbers. The raw infrared images were converted to temperature via a radiometric calibration of the camera sensor. Corrections were made for losses due to test article emissivity and window transmissivity. A preliminary uncertainty analysis yielded an estimated accuracy within 4 K at moderate viewing angles, similar to that of a standard thermocouple. Surface heat flux was obtained from the measured surface temperatures via a finite-difference solution of the one-dimensional heat equation that modeled thermal variation of the material properties. Comparisons of the measured heating to both computational and theoretical predictions demonstrated agreement within the expected uncertainty of the technique. The heat transfer measurement near the stagnation point was found to be highly sensitive to the test article emissivity, which establishes the need for improved characterization of the wind tunnel model materials for high temperature applications.

I. Nomenclature

B, F, G, R	=	radiometric calibration coefficients
c_1, c_2	=	first and second radiation constants
c_p	=	specific heat capacity of air
c_x, c_y	=	principal point coordinates
f_x, f_y	=	focal lengths
h	=	heat transfer coefficient
I	=	radiance
K	=	camera intrinsic matrix
M_∞	=	freestream Mach number
n	=	refractive index
$\hat{n}$	=	surface normal vector
p	=	pressure
q	=	heat flux
R, t	=	camera extrinsic parameters
Re	=	freestream unit Reynolds number
s	=	arc distance from the stagnation point
T	=	temperature
U	=	infrared image counts
u, v	=	image coordinates
$\vec{w}$	=	camera vector in world coordinates
w_λ	=	infrared sensor spectral response

*Research Aerospace Engineer, Aerothermodynamics Branch, Member AIAA
†Research Aerospace Engineer, Aerothermodynamics Branch, Member AIAA
‡Research Aerospace Engineer, Aerothermodynamics Branch, Student Member AIAA

X, Y, Z	=	world coordinates
$\varepsilon_n, \varepsilon_\theta$	=	normal and directional emissivity
θ	=	camera viewing angle relative to the surface normal
λ	=	wavelength
ρ	=	density
τ	=	transmissivity

Subscripts

0	=	stagnation condition
∞	=	freestream condition
a	=	ambient
bb	=	blackbody
FR	=	Fay-Riddell
s	=	surface
w	=	window

II. Introduction

Aeroheating measurements in hypersonic wind tunnels provide important information to vehicle designers about surface heating rates, shock-boundary layer interactions, and boundary-layer transition. These factors are crucial for the design of thermal protection systems (TPS) which are necessary to survive the intense aerothermal environment of sustained hypersonic flight. The hypersonic ground test facilities at the NASA Langley Aerothermodynamic Laboratory (LAL) have been key to the development of reusable, air-breathing hypersonic vehicles and advanced TPS concepts for atmospheric reentry. Over the last three decades, the two-color, relative-intensity phosphor thermography methodology developed at NASA Langley Research Center has been the primary technique for global aeroheating measurements in LAL facilities [1]. This revolutionary technique enabled accurate global measurements at a significant cost reduction over discrete sensors. In combination with a unique fused silica ceramic slip casting method, phosphor thermography made it possible to rapidly transition from concept to test in a matter of weeks at relatively low cost. However, coating-based thermography techniques, such as phosphor thermography and temperature-sensitive paint, often suffer from a narrow operable temperature range and inherent limitations on resolution [2]. The current phosphor technique has a usable temperature range of 295-440 K with an asymptotic uncertainty as the surface temperature approaches ambient conditions [1]. This can make the technique ill-suited for slender geometries with lower heating rates or for the elevated temperatures expected at higher Mach numbers.

In recent years, infrared (IR) thermography has been widely used to accurately measure surface temperatures with high sensitivity [3]. Recent advances in infrared sensor technology have resulted in robust, high-resolution cameras that are able to resolve temperature differences to within 30 mK. The primary advantage of IR over other techniques is that the working spectral band and integration time can be tuned to suit a specific scene. This ensures high signal-to-noise and near constant uncertainty over the full temperature range. The application of IR to surface temperature and heat flux measurements in wind tunnels is not novel, and over the years, general procedures have been established for calibration, data acquisition, and correction for environmental factors in cold flow facilities [4]. The purpose of the current work is to demonstrate progress on the development of a quantitative IR technique for use in the LAL 20-Inch Mach 6 Air Tunnel and 31-Inch Mach 10 Tunnel. Procedures for calibration and temperature correction are provided along with measurements from a recent validation test campaign.

III. Hemisphere Experiment

A canonical hemisphere geometry was chosen for this validation study so that measurements can be compared to theory, computations, and prior experiments. A 4-inch (101.6 mm) diameter hemisphere has been frequently used as a check standard for the phosphor thermography technique in LAL facilities, so ample historical data are available for comparison [1]. A secondary objective of this test campaign was to identify suitable materials for hypersonic wind tunnel models which require durability at high temperatures. Hemisphere models were fabricated from three low-conductivity, high-emissivity materials: polyether ether ketone (PEEK), Formlabs Rigid 10K, and a slip-cast fused silica ceramic. PEEK has a history of use for IR measurements in hypersonic tunnels, and its material properties are

fairly well characterized [4–7]. Formlabs Rigid 10K is a highly glass filled stereolithography 3D printing material which has seen increased use for wind tunnel models in recent years due to its low cost and ease of manufacture [8–11]. These two hemispheres are shown in Figure 1. A third model, shown in Figure 2, was fabricated via the traditional slip-cast fused silica ceramic process used for phosphor thermography models [1, 12]. The sting mount for this model necessitated the addition of a 5° half-angle conical flare to the aft end of the hemisphere.

Fig. 1 PEEK (left) and Formlabs Rigid 10K (right) hemisphere models instrumented with Ahmic Aerospace high-speed temperature gauges.

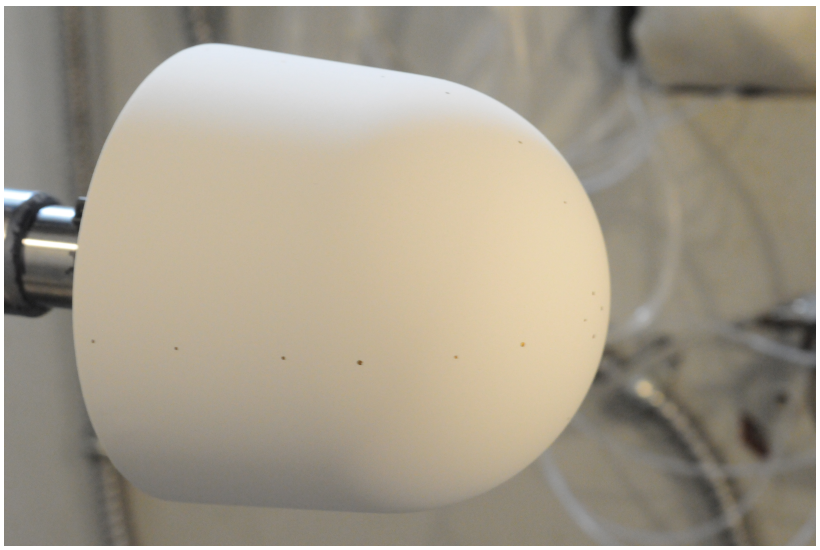

Fig. 2 Slip-cast fused silica ceramic hemisphere-flare model mounted in the injection box beneath the test section.

A. Instrumentation

The PEEK and Rigid 10K hemispheres were instrumented with Ahmic Aerospace high-speed temperature gauges [13]. They were potted directly into the model along a single arc at 0°, ±15°, ±30°, and ±60° azimuthal angles from the stagnation point. Calibrations from the manufacturer were supplied with the gauges to convert measured voltages to

temperatures. The original intent was to use these gauges for validation of the global IR heat flux; however, uncertain material properties and three-dimensional conduction effects made reduction to heat flux impractical. Instead, these gauges were primarily used to monitor pre- and post-run temperatures and to evaluate surface temperature trends during model injection. For brevity, no data from these gauges are presented. A T-type thermocouple was embedded inside each model to monitor the internal temperature for use as a backface condition in IR data reduction process. The ceramic hemisphere did not have integral instrumentation. Instead, a beaded T-type thermocouple was placed on the aft surface to provide an estimate of the internal model temperature.

B. 20-Inch Mach 6 Air Tunnel

The LAL 20-Inch Mach 6 Air Tunnel is a conventional blowdown facility with a fixed-geometry, two-dimensional nozzle. A schematic of the tunnel and associated infrastructure is shown in Figure 3. The top and bottom walls of the nozzle are contoured, and the side walls are parallel. Air is supplied from a high-pressure bottle field and is resistively heated to a maximum temperature of 550 K. The facility can operate at freestream Reynolds numbers between 1.2×10^6 m^{-1} and 27.9×10^6 m^{-1} and for test durations as long as 20 minutes. For surface heating measurements, typical run times are approximately 30 seconds with the model at the tunnel centerline for 5-10 seconds. Freestream conditions for the current measurements are provided in Table 1. To reduce model loads during start-up, the models are injected into the freestream once the tunnel has established steady operating conditions. The model is injected into a 20" × 20.5" (508 mm × 521 mm) test section, which has optical access via top- and side-mounted windows. A zinc selenide (ZnSe) window was installed into the top of the test section for the present IR measurements. A more detailed description of the facility's infrastructure and test capabilities can be found in Reference [12].

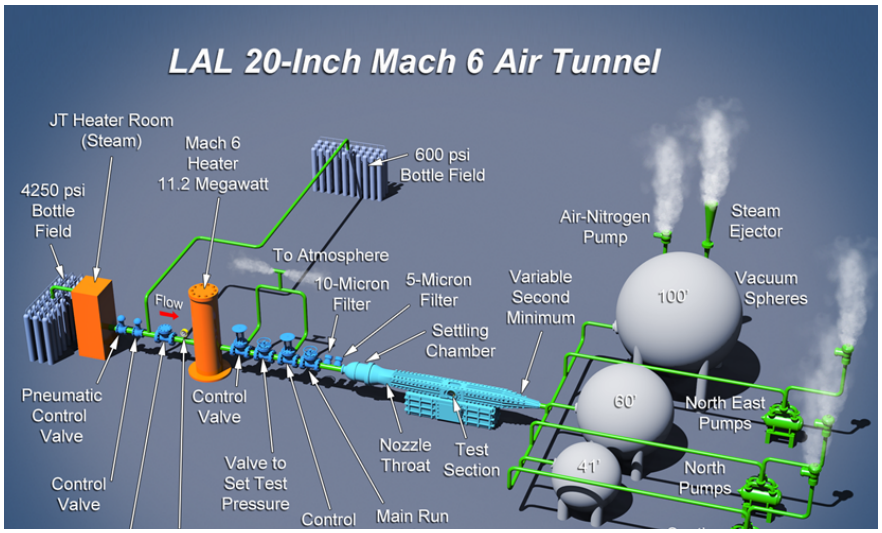

Fig. 3 Schematic of the LAL 20-Inch Mach 6 Air Tunnel.

Table 1 Average freestream conditions.

M_∞	p_0, MPa	T_0, K	p_∞, Pa	T_∞, K	ρ_∞, kg/m^3	$Re \times 10^6$, m^{-1}
5.96	0.868	504.7	576.8	62.5	0.0322	6.78
6.01	1.733	505.5	1109.4	61.9	0.0626	13.32
6.02	2.258	519.8	1422.8	63.4	0.0784	16.53
6.03	2.534	519.7	1590.6	63.3	0.0878	18.53
6.04	2.947	519.9	1841.8	63.2	0.1017	21.51
6.04	3.286	519.9	2048.0	63.2	0.1133	23.97

IV. Surface Temperature Reconstruction

In order to obtain a global measurement of the surface heat flux, a three-dimensional temperature field must first be reconstructed from the infrared images. This process begins with the acquisition of images using an IR camera with an appropriate working bandwidth and integration time. Figure 4 shows blackbody spectra for temperatures one might expect to observe in cold flow wind tunnels. Superimposed on these spectra are typical working bandwidths for mid-wavelength (MWIR) and long-wavelength (LWIR) cameras. For lower surface temperatures, the LWIR camera provides the strongest signal integrated over the bandwidth. For higher surface temperatures, this advantage gradually transitions towards the MWIR band. Given the shape of the spectra, a MWIR camera will generally have better thermal contrast for the temperatures considered here. Both bandwidths should provide adequate signal in this temperature range assuming that the integration time is adjusted to make full use of the camera's dynamic range.

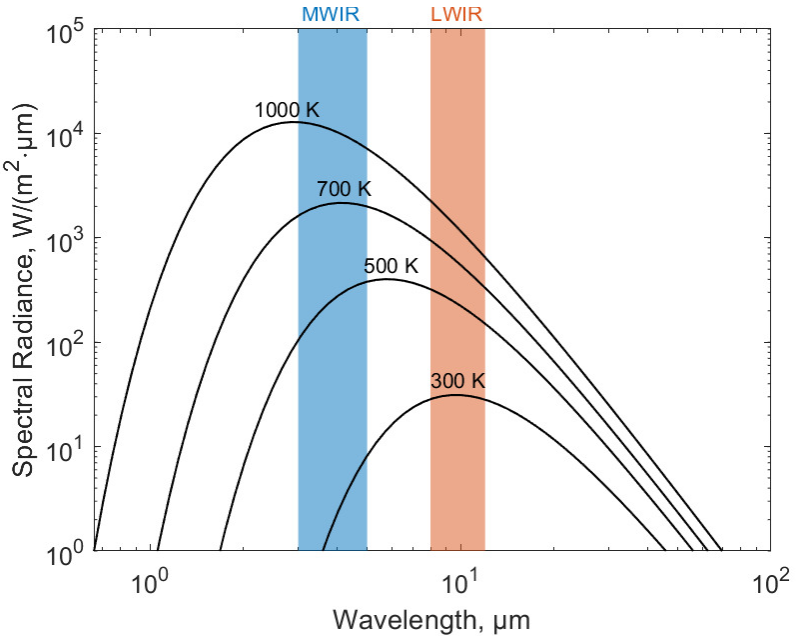

Fig. 4 Blackbody spectra for potential surface temperatures in LAL facilities.

An IR image is a measure of the total radiation detected by the IR sensor, which is the sum of many different sources. Figure 5 shows a diagram of an IR scene representative of a typical aeroheating study in a wind tunnel. The camera is pointed at a wind tunnel model, which resides in the tunnel test section. An IR-transparent window is mounted in the tunnel wall to provide optical access to the model. In the absence of the window and under the assumption that atmospheric transmission losses are negligible over the distances between the components, the total radiant flux measured by the sensor is the sum of the radiation emitted by the body, I_s, and the portion of the ambient radiation, I_a, reflected from the model surface. The model material is assumed to be a graybody with a constant emissivity, ε, across the spectral range of the IR sensor. The window material is typically chosen to have excellent transmission in the bandwidth of the camera and is anti-reflective (AR) coated to further increase transmission. Even so, some small percentage of the radiation emitted and reflected from the model surface is absorbed by the window and some correspondingly small fraction of radiation is emitted by the window, I_w. Equation 1 details the summation of all sources collected by the IR camera [3].

$$I = \tau\varepsilon I_s + \tau(1-\varepsilon)I_a + (1-\tau)I_w \tag{1}$$

Window transmission losses are generally assumed to be quite small, or at the very least can be accounted for in the radiometric calibration of the IR camera. The AR coating of the window used in this study is not ideally suited for the chosen camera. So, the transmission term, τ, is carried forward in the analysis. For the flush-mounted window used for the present work, an assumption is made that the window temperature and temperature of the ambient environment (i.e. tunnel walls) are approximately equal, $I_w = I_a$. Simplifying and rearranging Equation 1 yields the simple expression in

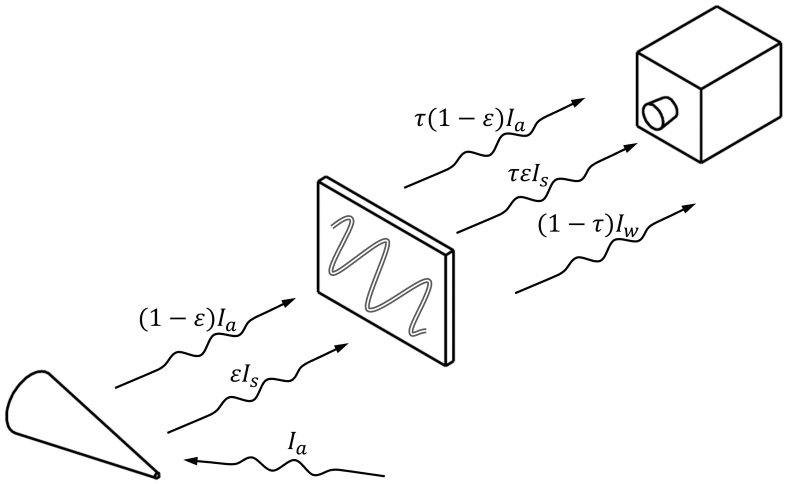

Fig. 5 Simplified diagram of the radiation measured by the IR camera.

Equation 2 for the portion of the radiant flux collected by the camera that is attributed to the model surface. In order to determine an accurate surface temperature from an IR image, one must characterize the radiometric response of the IR camera, the emissivity and transmissivity of all components in the optical path, and all possible ambient sources of radiation.

$$I_s = \frac{I - (1 - \tau\varepsilon)I_a}{\tau\varepsilon} \tag{2}$$

A. Image Acquisition

The measurements in the present work were acquired with an actively-cooled, research-grade infrared camera manufactured by Teledyne FLIR. Specifications for the IR camera are listed in Table 2, including the spectral band, sensor resolution, and noise equivalent temperature difference (NETD). Although a MWIR camera would provide better sensitivity for the expected temperatures and the tunnel's ZnSe window can transmit the appropriate wavelengths, an LWIR camera was chosen because the AR coating was tailored for an 8-12 µm bandwidth. The camera was mounted above the tunnel window and oriented to minimize the camera angle into the stagnation point of the hemisphere. A 50 mm f/2.5 lens was used to provide a tight field of view (FOV) and a working distance of approximately 1 meter. Data acquisition for the camera and tunnel data system were initiated manually from a single trigger. The model was injected into the test section approximately 1 second after the trigger so that discrete temperature gauge data could be gathered prior to and during injection. Images were acquired for 10 seconds at a 15 Hz frame rate.

Table 2 IR camera specifications.

	FLIR SC6701SLS
Sensor	SLS
Spectral Range	7.5-9.5 µm
Resolution	640×512
NETD	<30 mK
Lens	50 mm f/2.5
Frame Rate	15 Hz
Integration Time	0.1643 ms

B. Radiometric Calibration

Each photodiode in the camera's focal plane array (FPA) generates a voltage in response to incident radiation. These voltages are passed to an analog-to-digital converter and returned as 14-bit count values for each pixel. A radiometric calibration of the sensor is performed to convert the measured counts into units of interest. In most cases, the measured counts are first converted to in-band radiance since the relationship between these two values is highly linear. A linear fit would be obtained between image counts of a blackbody at a known temperature and the apparent radiance of the blackbody. The apparent radiance of the blackbody can be determined from integration of Planck's law, as shown in Equation 3, which includes a correction for the emissivity of the blackbody. The temperature is then obtained from the radiance value via a look-up table. Note that this method requires characterization of the sensor's spectral response, w_λ, which is not always known and can vary with the lens and with the age of the sensor.

$$I = \int_{\lambda_1}^{\lambda_2} \frac{c_1 w_\lambda}{\lambda^5} \left[\frac{\varepsilon_{bb}}{\exp\left(c_2 \lambda T_{bb}\right) - 1} + \frac{1 - \varepsilon_{bb}}{\exp\left(c_2 \lambda T_a\right) - 1} \right] d\lambda \tag{3}$$

A simpler method, which is implemented in this work, is to use a Planckian model to directly relate counts, U, to temperature, T. A modification of the Sakuma-Hatori equation shown in Equation 4 is used in this work, as proposed by Zaccara et al. [4]. This equation is analogous to Planck's law and includes four coefficients which are computed via a non-linear least squares fit to calibration data. R is representative of the chosen integration time and spectral response of the sensor, B is a function of the spectral response of the sensor, and F should be near unity. The constant, G, is included to improve the quality of the curve fit and to nominally account for factors such as the non-uniformity correction (NUC) and transmission losses.

$$U = \frac{R}{\exp\left(B/T\right) - F} + G \tag{4}$$

The LWIR camera was calibrated in a benchtop setting in reference to an Infrared Systems IR-564 cavity blackbody with a 0.6-inch diameter aperture. Specifications for the blackbodies used in this work are listed in Table 3. For each calibration point, the blackbody was allowed to remain at the set temperature for at least 30 minutes to reach equilibrium and ensure peak uniformity across the aperture. Prior to the first point, an internal NUC was performed. This is critical because a single calibration is applied to all pixels in the FPA as opposed to performing the calibration on a per-pixel basis. Images of the blackbody were obtained at a 15 Hz frame rate over 10 seconds, yielding a total of 150 frames per temperature setpoint. Figure 6 shows an example blackbody frame along with a histogram of the counts measured across the cavity for all 150 calibration frames. The counts are normally distributed with a standard deviation of 2-3% of the mean depending on the set temperature. Values for each pixel are stable within a few counts over the duration of the measurement, indicating that the distribution is reflective of the spatial uniformity of the measurement. It is unclear whether this is due to uniformity of the blackbody or uniformity of the sensor, although the distribution does not appreciably contribute to the overall uncertainty of the calibration curve fit.

Table 3 Blackbody calibration source specifications.

	IR 564/301	IR 2101/301
Type	cavity	flat plate emitter
Range	50–1200 °C	-30–75 °C
Resolution	0.1 °C	0.1 °C
Accuracy	±0.2 °C	±0.2 °C
Stability	±0.1 °C	±0.1 °C
Emissivity	>0.99	0.96 ± 0.02

The radiometric calibration coefficients in Equation 4 are generated via a fit to calibration data over a range of temperatures. A calibration curve is shown in Figure 7 for the LWIR camera with a 0.1643 ms integration time which provides a sufficient dynamic range to encapsulate the expected temperature range for the hemispheres. The nominal counts are the mean value of the calibration frames. The nominal temperature is the apparent temperature of the blackbody. This was determined via the Stefan-Boltzmann scaling in Equation 5 which corrects the blackbody temperature provided by an internal RTD for the emissivity of the cavity. The response of the sensor is linear between

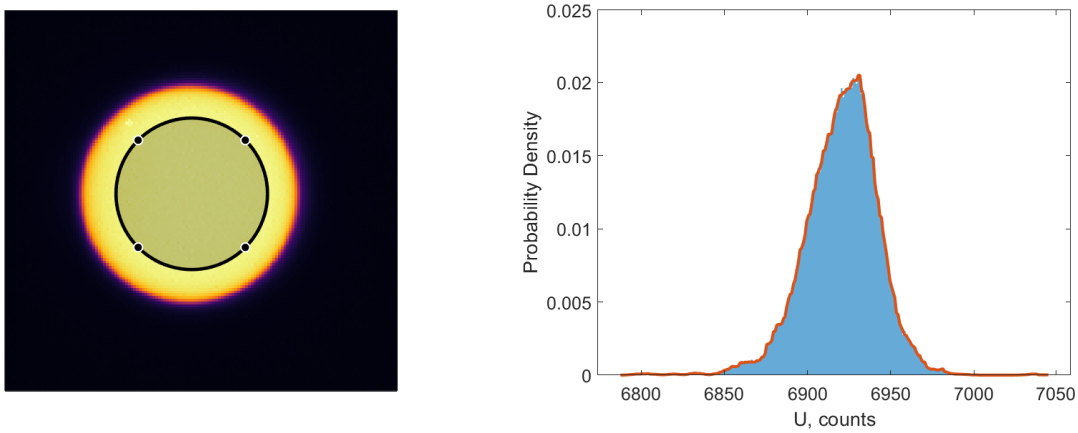

(a) IR image of cavity blackbody **(b) Histogram of measured counts**

Fig. 6 Example measurement of blackbody calibration frame.

20% and 80% of the dynamic range, so points were only included in the curve fit when the mean count value from calibration frames was between approximately 3000 and 13000. A Monte-Carlo analysis was performed to estimate the uncertainty of the curve fit to the calibration data. The nominal calibration points were perturbed according to the uncertainty budget in Table 4 with draws on the blackbody temperature, the blackbody emissivity, the ambient temperature, and the image counts. A fit was generated to the perturbation cloud via a non-linear least-squares fit using the Levenberg-Marquardt method. The resulting coefficients are summarized in Table 5 along with the 95% prediction interval of the fit.

$$T^4 = \varepsilon_{bb} T_{bb}^4 + (1 - \varepsilon_{bb}) T_a^4 \tag{5}$$

Table 4 Uncertainty budget for the radiometric calibration (N = 10,000).

Parameter	Standard Unc.	Source	Type	Distribution
blackbody temperature, T_{bb}	0.2 K	RTD	Systematic	Uniform
blackbody emissivity, ε_{bb}	0.003	Manufacturer	Systematic	Uniform
ambient temperature, T_a	2 K	Thermocouple	Systematic	Uniform
counts, U	Varies*	Camera	Random	Normal

*St. dev. of calibration frames

Table 5 Radiometric calibration curve fits.

Integration time	0.1643 ms
R	510780
B	1587.7
F	1.6223
G	1026.7
$u_{95\%}$: forward	62.7 counts
$u_{95\%}$: reverse	0.71 K

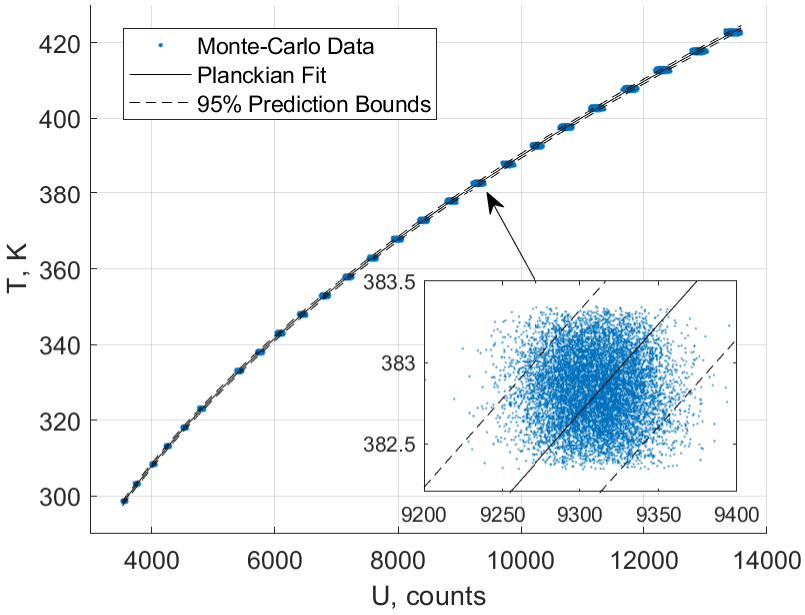

Fig. 7 IR camera calibration curve and uncertainty bounds.

The radiometric calibration of the camera was generated in a benchtop setting without the window between the camera and the blackbody. As noted previously, transmission losses through the tunnel window can typically be accounted for during calibration. In this case, it was impracticable to install a high quality cavity blackbody into the test section. Instead, an effort was made to characterize the transmissivity of the ZnSe window integrated over the bandwidth of the sensor, and any losses could then be accounted for via the transmission term in Equation 2. The ZnSe window used for these measurements is coated on both sides to reduce reflections with optimal performance in the 8-12 µm bandwidth. The spectral range of the LWIR camera used in this study is 7.5-9.5 µm which does not completely fall within with the fully-characterized range of the window. Measurements from the manufacturer in Figure 8 indicate an average transmissivity of 0.987 for wavelengths between 8 and 9.5 µm, but the roll-off between 7.5 and 8 µm is expected to significantly decrease the effective transmission. An in-situ calibration with a small format blackbody was performed to estimate the transmission over the bandwidth of the sensor. An Infrared Systems IR-2101 flat plate emitter blackbody was placed in the test section with the blackbody surface near the flow centerline. As noted in Table 3, the temperature of this blackbody was limited to 348 K and could not be used to perform a full calibration over the necessary temperature range. An in-situ calibration curve was generated for temperatures between 288 K and 348 K using the procedure described above. Figure 9 shows a comparison of the curve fits for the in-situ and benchtop calibrations. As expected, when a measurement is made in-situ, the counts are lower for a given temperature due to window transmission losses. Performing a similar analysis to that in Equation 1, the transmissivity of the window can be estimated from the two curve fits via Equation 6. The effective transmissivity of the window was determined to be approximately 0.96 and was used for all subsequent transmission corrections.

$$\tau = \frac{U_{in-situ} - U_a}{U_{bench} - U_a} \tag{6}$$

C. Spatial Calibration

The emissivity of the wind tunnel model at any given pixel is a function of the camera viewing angle relative to the surface normal vector at the surface coordinate corresponding to that pixel. A pinhole camera model was used to estimate the intrinsic and extrinsic camera parameters necessary to map the model surface, determine the viewing angle, and perform the temperature correction for directional emissivity. The calibration algorithm used for this work includes the pinhole camera model in addition to corrections for tangential and radial distortions [14–16]. Equations 7 and 8 define the pinhole model and intrinsic matrix. World coordinates, (X, Y, Z), are transformed to

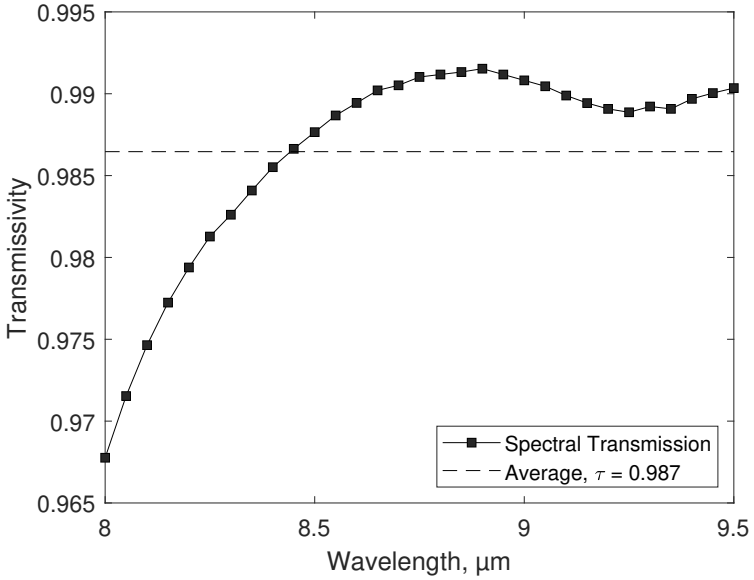

Fig. 8 Manufacturer measurements of the ZnSe window spectral transmission.

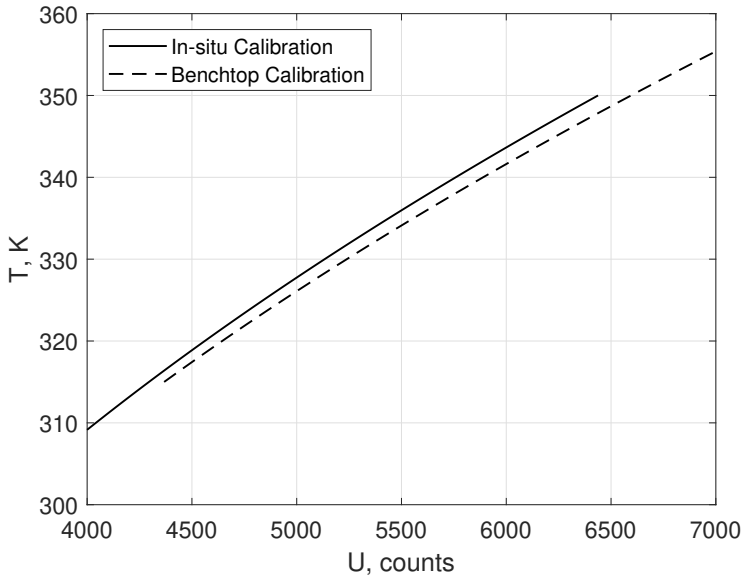

Fig. 9 Comparison of the radiometric calibration curves between the benchtop and in-situ.

image coordinates, (u, v), via the camera's rotation and translation matrices, R and t, in addition to the intrinsic matrix, K. Adjustments are made for tangential and radial distortions using two-coefficient models, although distortions are expected to be minimal for the 50 mm focal length lens used in this work. The calibration algorithm estimates the intrinsic and extrinsic parameters based on a set of known three-dimensional (3D) world points and their corresponding two-dimensional (2D) image coordinates, which are typically generated from images of a specially designed calibration target. A non-linear optimization algorithm is utilized to determine the camera's intrinsic and extrinsic parameters which minimize reprojection errors of the calibration points.

$$\begin{bmatrix} u \\ v \\ 1 \end{bmatrix} = K \begin{bmatrix} R & t \end{bmatrix} \begin{bmatrix} X \\ Y \\ Z \\ 1 \end{bmatrix} \tag{7}$$

$$K = \begin{bmatrix} f_x & s & c_x \\ 0 & f_y & c_y \\ 0 & 0 & 1 \end{bmatrix} \tag{8}$$

For this work, a specialized calibration target had to be designed such that the keypoints could be easily found via grid detection algorithms. A polished aluminum plate was fabricated with an asymmetric grid of 2.4-mm-diameter holes to act as the target points with a standard spacing of approximately 19 mm. The holes were drilled sufficiently deep relative to the diameter such that they acted as blackbodies. The difference in emissivity between the holes and the polished surface provided sufficient contrast when heated via silicone heaters adhered to the backside of the plate. The holes were sized such that even for a small FOV there would be at least 5 pixels across the diameter, which is a general requirement for a robust point detection algorithm. As shown in Figure 10, the calibration target was sting mounted using the same struthead as the hemisphere models. This ensures that only a simple translation is required to relate the calibration coordinate system to the model coordinate system. During calibration, the plate was injected into the test section and rotated through a range of angles of attack and yaw using the tunnel's arc sector.

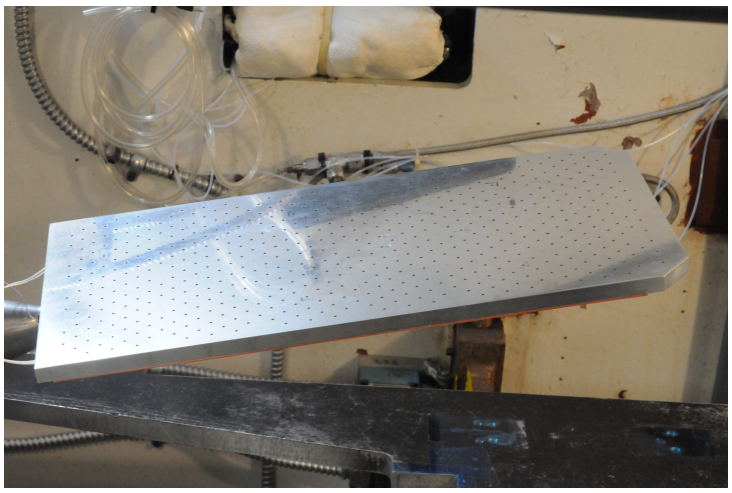

Fig. 10 Sting-mounted calibration target in the injection box beneath the test section.

An example IR image of the calibration target is shown in Figure 11. The grid detection algorithm used to identify the keypoints, shown in blue, utilizes a 2D cross-correlation to detect the centroid of the target points with sub-pixel resolution. The calibration target was designed to work for models significantly larger than the hemispheres considered in this work, so only a subset of the points on the plate were used. This same pattern of points was detected in 42 total calibration images. The angles of attack and yaw for the calibration images were chosen such that the calibrated volume fully encapsulated the region of the test section in which the hemispheres were mounted. The extracted 2D-image coordinates and their corresponding 3D-world coordinates were passed to the calibration algorithm and camera parameters were generated. Figure 12 shows the reprojection error of the resulting calibration for each of the calibration images. The overall mean reprojection error is approximately 0.06 pixels. Based on the spatial resolution of the calibration images, an average of 10 pixels across the diameter of the target points, this equates to a reprojection error of approximately 14 µm. Repeated calibrations showed negligible variation in the extracted target points or estimated camera parameters.

The final step of the spatial calibration process is to determine the relationship between the calibration coordinate system and the model coordinate system. The calibration plate was sting-mounted using the same strut bore as the hemisphere, so the coordinate system transformation should just be a simple translation. The offsets between the

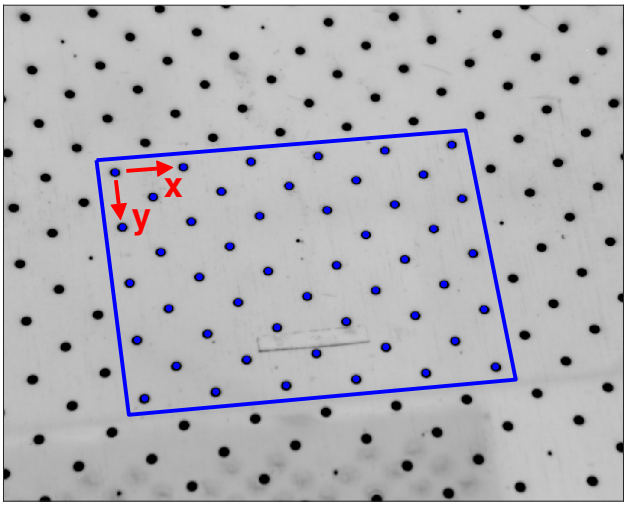

Fig. 11 Calibration target with area of interest highlighted in blue.

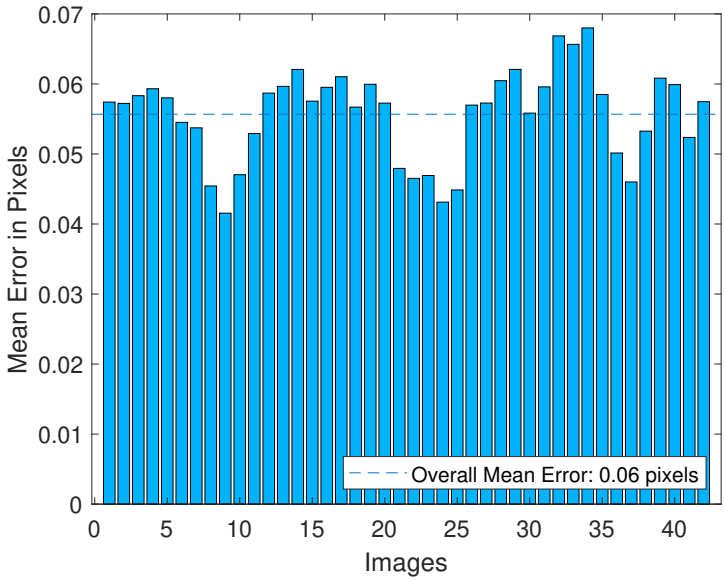

Fig. 12 Camera calibration reprojection errors.

calibration coordinate system origin, shown in red in Figure 11, and the sting axis are known. However, the translation along the streamwise direction, or the y-direction in Figure 11, depends on the total length of the model sting that was mounted in the strut. To determine this streamwise offset, a 3D point cloud representing the theoretical model surface was placed into the world coordinate system and then super-imposed via the pinhole camera model onto an IR image of the hemisphere. The point cloud was then translated along the streamwise direction until the imported mesh points aligned with the gold ink fiducial markers placed at known locations on the model surface. Figure 13 shows an example of a mapped image with an intentionally sparse point cloud to provide clarity. A 3D reconstruction of the scene is also provided to illustrate the orientation and position of the camera relative to the hemisphere model. In this 3D scene, the colormap has been assigned such that any point on the surface that is within view of the camera is red. With the model

surface successfully mapped, the viewing angle at each pixel can be determined from the surface normal vectors, $\hat{n}$, and camera vectors, $\vec{w}$, via Equation 9. Figure 14 shows the resulting camera viewing angle superimposed on a mapped IR image. This view is oriented downstream and shows that the camera viewing angle near the stagnation point is less than 60°.

$$\theta = \arccos\left|\frac{\vec{w}\cdot\hat{n}}{\|\vec{w}\|}\right| \tag{9}$$

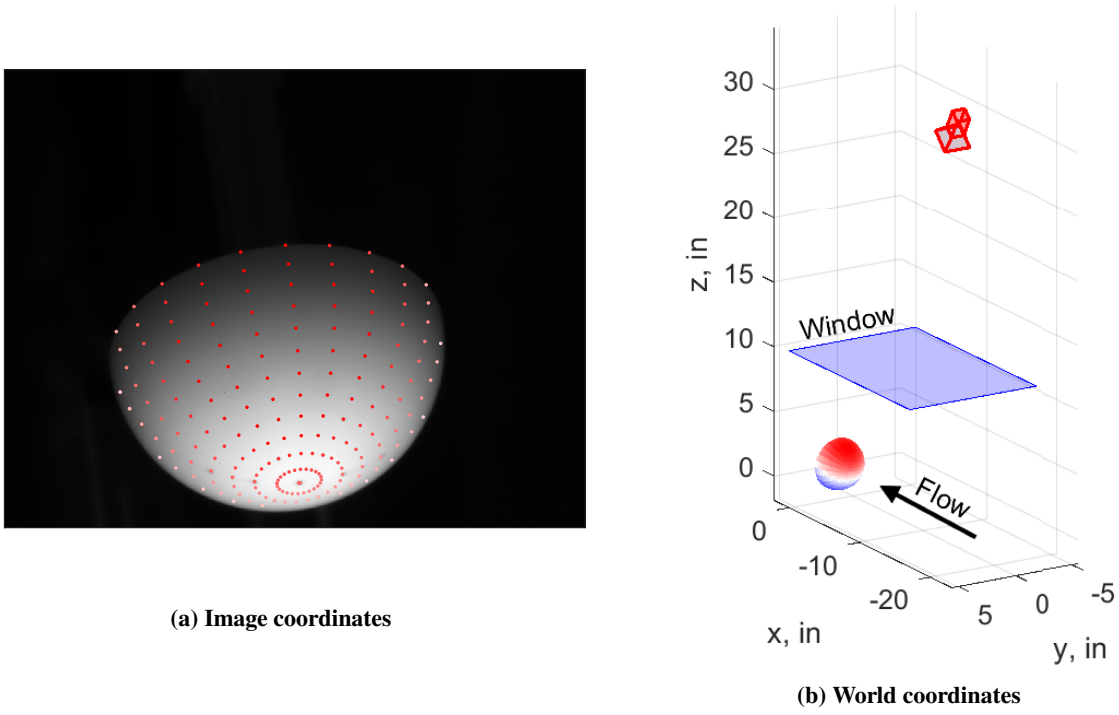

(a) Image coordinates

(b) World coordinates

Fig. 13 Surface mapping and camera extrinsic parameters.

There are many possible sources of uncertainty in the viewing angle, such as the camera parameters, misalignment between the sting and either the calibration plate or the model, and unknown variation in the injection system position between runs. In order to estimate the uncertainty of the camera viewing angle, an analysis has been conducted considering only first order effects. For the present analysis, only the camera parameters and the spatial resolution on the mapped model surface have been considered. The contribution of the camera intrinsic parameters to overall viewing angle uncertainty is expected to be small due to the relatively long focal length of the 50 mm lens and is therefore neglected. The camera calibration algorithm generates a standard uncertainty for the camera's position and rotation as an output of the non-linear optimization. Based on these standard uncertainties, the estimated standard angular uncertainty of the camera vector is approximately 0.61°. The angular uncertainty due to the spatial resolution of the mapped model surface was estimated as half of the angular width of each pixel. In this case, the angular width is determined from the change in the surface normal vector across the pixel width. This uncertainty is plotted in Figure 15 as a function of the nominal viewing angle. Obviously, as the viewing angle becomes steeper, the spatial resolution is reduced and the angular uncertainty increases. The total angular uncertainty was evaluated from the extrinsic parameters and resolution uncertainties using the typical root-sum-square method for independent sources. This total uncertainty is also plotted in Figure 15. In general, the viewing angle uncertainty is nearly constant up to approximately 60°.

D. Surface Temperature Correction

To implement the corrections in Equation 2, the spectral directional emissivity for a given material must be known. The normal emissivity is primarily a function of the refractive index of a material, but can also be affected by other

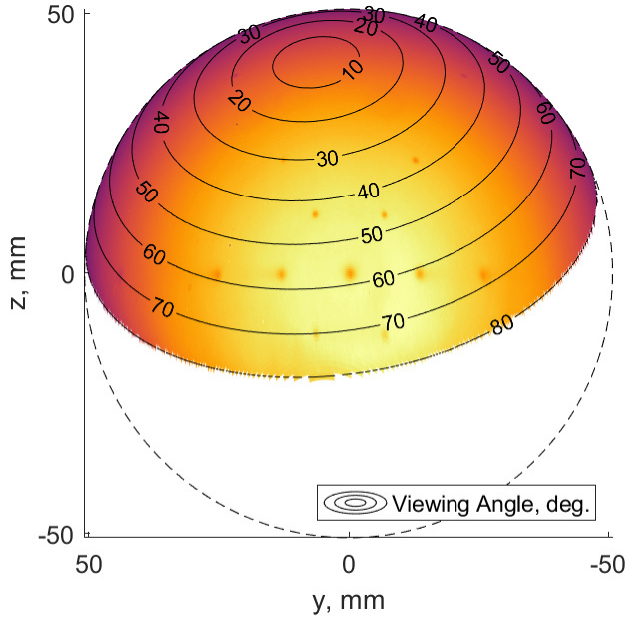

Fig. 14 Camera viewing angle superimposed onto the mapped IR data.

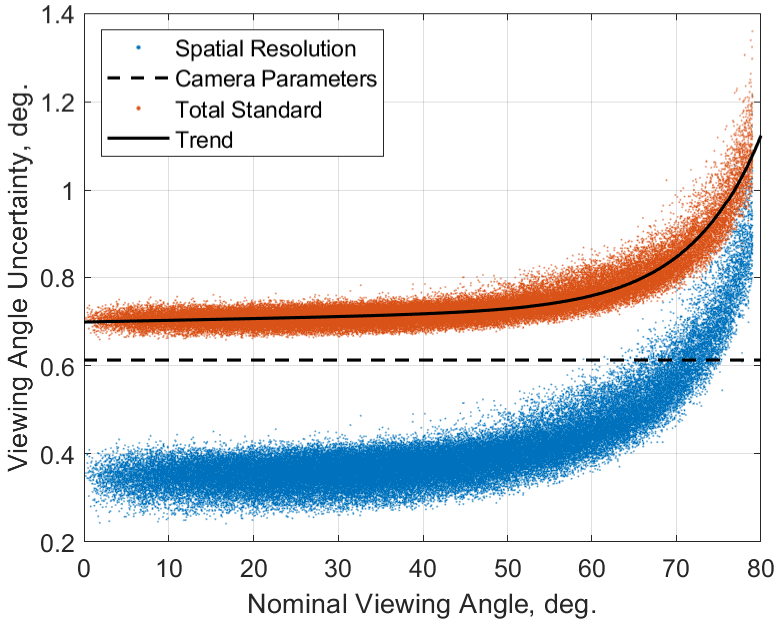

Fig. 15 Standard uncertainty of the viewing angle.

factors related to the overall quality of the surface. There are many methods to determine the emissivity using a representative sample of a material, some of which are being evaluated at NASA LaRC in relation to this IR development effort. However, this representative sample may not fully capture the surface finish of the wind tunnel model and does not account for changes in emissivity throughout a wind tunnel test that might occur due to accumulation of contamination, particle impacts, and thermal cycles above the glass transition temperature. As a result, a fair assessment would suggest that the spectral emissive properties of the three materials used in this study are not well-characterized. PEEK has a long

history of use for IR measurements in wind tunnels and several values for the normal emissivity exist in the literature that range from 0.91 to 0.95 [4–6]. Reflectance-based measurements of PEEK samples were performed for this work using a Surface Optics Corporation ET-100 handheld emissometer, which yielded an average normal emissivity of approximately 0.94±0.002. There are far fewer measurements available in the literature for the other model materials. A measurement of the Formlabs Rigid 10K material using the handheld emissometer gave an average normal emissivity of 0.95±0.003 for several samples. Previous measurements of the fused silica ceramic suggest a normal emissivity of approximately 0.91. The nominal emissivity and refractive indices for each of the model materials are listed in Table 6.

For the purposes of the present study, all three materials are assumed to be opaque and to have graybody emission, or emission that is invariant with wavelength. The validity of the opaque and graybody assumptions is under question, especially for the fused silica ceramic and glass-filled Rigid 10K materials, but this will be evaluated in future work. From electromagnetic theory, the directional emissivity of opaque dielectric materials is a function of the refractive index and the viewing angle of the camera with respect to the surface normal. Equation 10 shows the relationship between emissivity and viewing angle for a specified refractive index, n [17]. For normal emissivity, where $\theta = 0$, the equation reduces to $4n/(n+1)^2$, where the refractive index typically varies between 1 and 4. Figure 16 shows the variation of emissivity with viewing angle relative to the surface for nominal values of the refractive index for the three model materials. These curves demonstrate that the emissivity is approximately normal up to around 45° and then drops off steeply between 60° and 80°. For complex scenes with steep viewing angles, as one might experience with a complex 3D geometry, these factors are crucial for an accurate reconstruction of the 3D temperature field.

$$\varepsilon_\theta = \frac{2cos\theta\sqrt{n^2 - sin^2\theta}}{(cos\theta + \sqrt{n^2 - sin^2\theta})^2}\left(1 + \frac{n^2}{\left(cos\theta\sqrt{n^2 - sin^2\theta} + sin^2\theta\right)^2}\right) \tag{10}$$

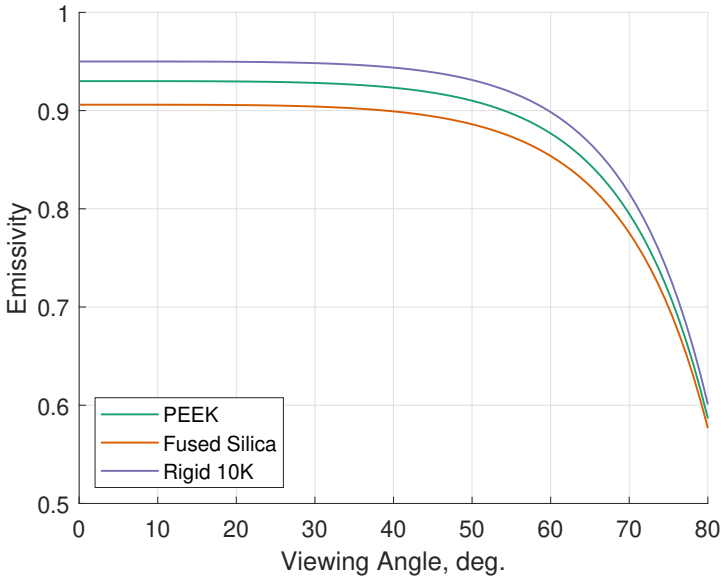

Fig. 16 Directional emissivity for the hemisphere materials.

Table 6 Material emissivity.

Material	ε_n	n
PEEK	0.91-0.95	1.58-1.86
Rigid 10K	0.95	1.58
Fused Silica	0.91	1.86

Recognizing that radiance is linear with image counts, the emissivity and transmissivity corrections in Equation 2 can be made directly to the raw IR measurements. After implementing the radiometric calibration for the surface and ambient values, Equation 2 can be rewritten to solve for the corrected surface temperature, T_s, as shown in Equation 11. The window transmissivity is applied uniformly to the entire image while the directional emissivity is evaluated at each pixel. The ambient temperature used for the correction is measured via a thermocouple mounted in the tunnel sidewall just upstream of the test section. Ambient sources are assumed to be uniform. While the ambient sources are likely not uniform due to a temperature distribution along the length of the nozzle, the window transmissivity and model emissivity are close enough to unity to make the correction relatively insensitive to the chosen value of T_a. A qualitative comparison of the corrected and uncorrected image counts is shown in Figure 17. The uncorrected image shows a reduction in image counts in the region below the stagnation point. This corresponds with a steep decrease in the directional emissivity with increased viewing angles, which is demonstrated by the superimposed line contour. After the correction, the distribution of image counts becomes radially uniform as would be expected for a hemisphere at 0° angle of attack.

$$T_s = \frac{B}{\ln\left[\frac{\tau\varepsilon_\theta R}{U - G - (1-\tau\varepsilon_\theta)\frac{R}{\exp(B/T_a)-F}} + F\right]} \tag{11}$$

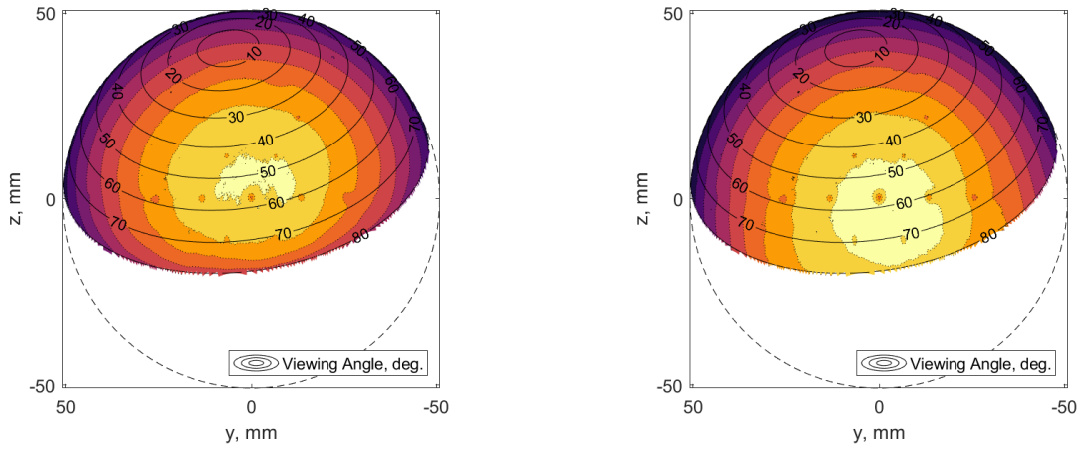

(a) Uncorrected **(b) Corrected**

Fig. 17 Qualitative comparison of uncorrected and corrected image counts.

Figure 18 shows an example surface temperature measurement mapped onto the surface of the hemisphere. This measurement was obtained for the PEEK model at a time late in the run at a freestream unit Reynolds number of 13.4×10^6 m^{-1}. The temperature uncertainty of this frame was estimated via a Monte-Carlo analysis. As detailed in Table 7, uncertainty draws were made on the ambient temperature, refractive index, and the viewing angle. The ambient temperature was treated as a systematic bias with a standard uncertainty even greater than a typical thermocouple uncertainty for conservatism. The refractive index was also treated as a systematic bias with a standard uncertainty representative of the variation in emissivity observed in the literature for PEEK. The viewing angle uncertainty is applied randomly to every pixel in the image based on the distribution in Figure 15. The radiometric calibration is used to convert the measured ambient temperature, T_a, to counts and then again to convert the corrected counts to the corrected surface temperature, T_s. For both instances, the calibration uncertainty was combined with the Monte-Carlo distribution via the root-sum-square method. The resulting total estimated uncertainty is plotted against the viewing angle in Figure 19. A colormap is applied to the points to show variation of the temperature uncertainty with the surface temperature. For viewing angles less than approximately 70°, the temperature uncertainty varies between 1 K and 3 K depending on the surface temperature, which is comparable to the uncertainty of a standard thermocouple. For viewing angles greater than 70°, the uncertainty steeply rises to a range that may render the measurement unusable depending on the application. The source of this uncertainty is largely attributed to low spatial resolution and a correspondingly high uncertainty in the directional emissivity.

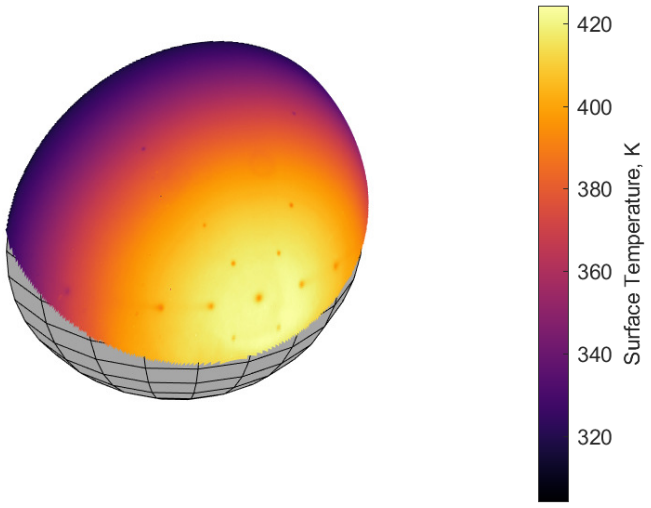

Fig. 18 Mapped surface temperature

Table 7 Uncertainty budget for the temperature Monte-Carlo analysis (N = 10,000).

Parameter	Standard Unc.	Source	Type	Distribution
radiometric calibration	0.36 K or 31.4 counts	Curve fit	Systematic	Normal
ambient temperature, T_a	5 K	Thermocouple	Systematic	Uniform
refractive index, n	0.14	Literature	Systematic	Uniform
viewing angle, θ	Varies*	Calibration	Random	Normal

*From Fig. 15

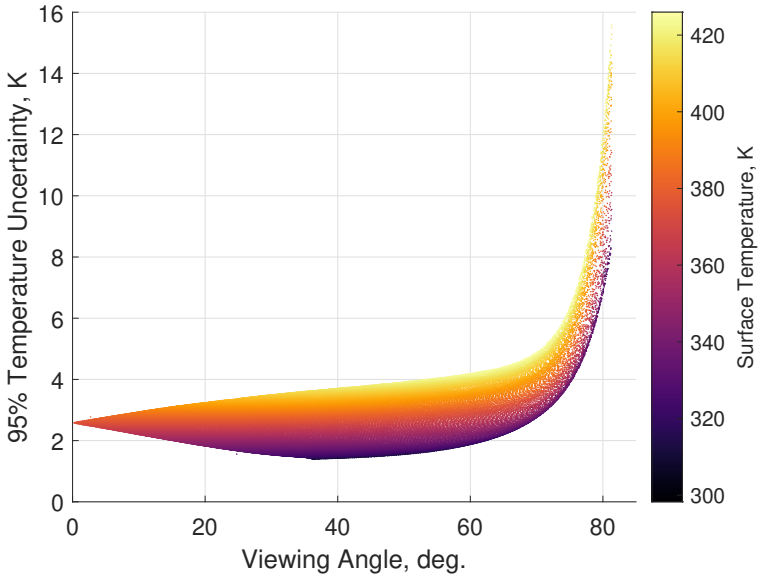

Fig. 19 Surface temperature uncertainty

V. Surface Heat Flux

Traditionally, aeroheating data in LAL facilities have been processed using an analytical semi-infinite method that utilizes a step function to approximate the heat transfer coefficient at some effective time after injection [1]. This method was computationally efficient, requiring only a pre-run image and an air-on image, but is limited by the step function approximatition in addition to assumptions of constant thermal properties and a semi-infinite wall. A finite-difference solver is used in the present work to permit less restrictive assumptions. The wind tunnel's model injection system introduces a challenge in the evaluation of heat flux because the surface temperature history is unknown between the initial pre-run image and the first air-on image with the model on the tunnel centerline. Recent work has progressed to evaluate methods of patching the temperature history between the pre-run image and the first air-on image [18]. A complex patch was developed to approximate the trends measured by thin film gauges which minimized any overshoot in the evaluation of heat flux, yielding converged solutions almost immediately after injection. A corresponding sensitivity study demonstrated that a simple linear interpolation between the pre-run data and the air-on data yielded similar results with minimal overshoot. For simplicity, the linear patch was used for the present work. An example time history is provided in Figure 20 for a location near the stagnation point.

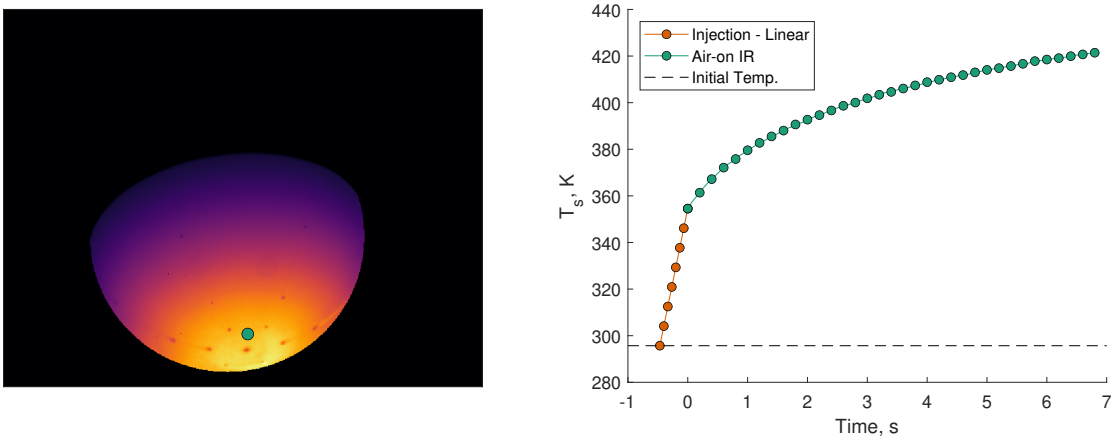

(a) Probed location **(b) Surface temperature time history**

Fig. 20 Example surface temperature history with injection.

The reconstructed surface temperature history at each pixel was reduced to heat flux via a finite-difference solution of the one-dimensional heat equation. The solver utilizes a Crank-Nicolson scheme that is second-order accurate in both time and space. The wall-normal domain makes use of node clustering near the surface of the model to increase computational efficiency. Given the high surface temperatures expected near the stagnation point of the hemispheres, the solver directly models thermal variation of the material properties at each node (i.e. conductivity and diffusivity). The thermal properties used for the heat flux calculation are provided in Figure 21 for each material. The PEEK thermal properties are from Häberle [6], the fused silica properties were measured by an external vendor [19], and the Rigid 10K properties were provided by researchers at the University of Arizona [20]. In all cases, the backface condition was assumed to be adiabatic, which should be appropriate given the wall thicknesses and test durations used for this experiment. Details of the solver including theory and validation cases can be found in Reference [18].

Dimensional heat flux data are converted to a pseudo heat transfer coefficient, h, as defined in Equation 12. Note that this definition substitutes the adiabatic wall temperature with the stagnation temperature, T_0. This is then normalized by the stagnation point heating predicted by a Fay-Riddell computation assuming a wall temperature of 300 K [21]. Using this normalization, the heating should be independent of the freestream Reynolds number.

$$h = \frac{q}{c_p(T_0 - T_s)} \tag{12}$$

An example output of the solver is presented in Figure 22 for the PEEK model at a freestream unit Reynolds number of 13.4×10^6 m^{-1}. The normalized heat transfer coefficient was probed at three locations and is plotted against the time during the run, where $t = 0$ seconds corresponds to the first frame with the model on the tunnel centerline. An overshoot in the heating is observed when the model reaches the tunnel centerline due to the discontinuity in slope of

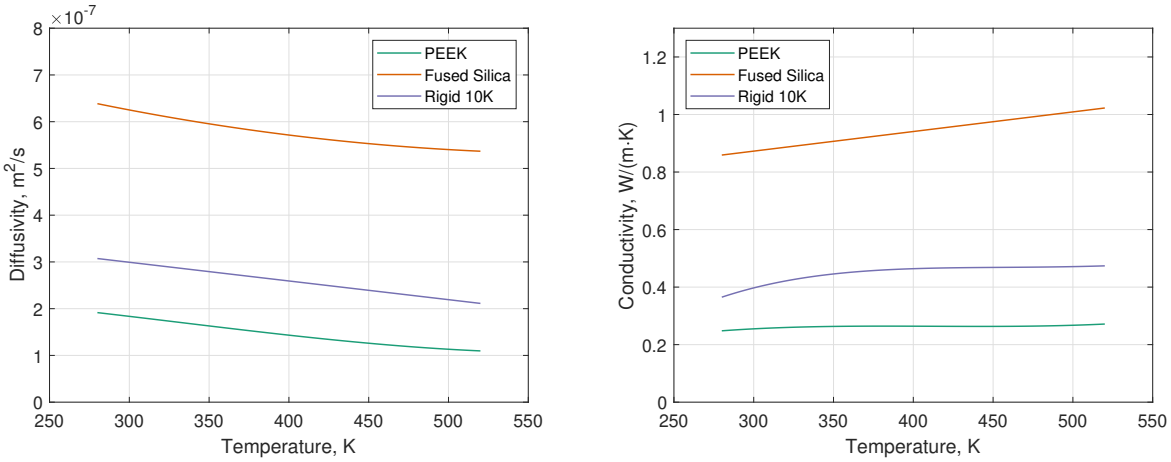

(a) Thermal diffusivity **(b) Thermal conductivity**

Fig. 21 Material thermal properties.

the temperature history caused by the linear interpolation during injection. This discontinuity is readily apparent in Figure 20. The overshoot is more pronounced for higher surface temperatures, but could be mitigated in future work by applying a more advanced patching method [18]. For all three locations, the heating collapses to a steady-state value approximately 1 second after the model reaches the tunnel centerline. The IR images are not spatially or temporally filtered, so there is some variability of the heating magnitude even after the steady state is achieved. This is also in part due to variation of the freestream properties throughout the duration of the run. To mitigate this variation, all subsequent heating data presented in this work are averaged over a 1 second duration centered about $t = 2$ seconds.

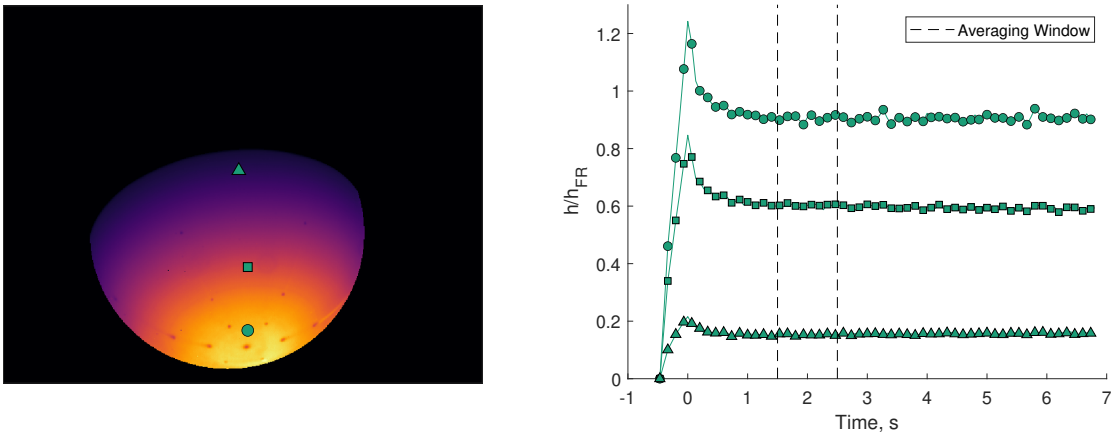

(a) Probed locations **(b) Surface heating time history**

Fig. 22 Temporal collapse of the normalized heat transfer coefficient for the Re = 13.4×10^6 m^{-1} case.

A. Surface Heating Results

Mapped surface heating data for the PEEK hemisphere at a freestream unit Reynolds number of 13.4×10^6 m^{-1} are shown in Figure 23. The data from each pixel are plotted as a function of the arc distance, s, from the stagnation point. Pixels have been ignored at which the camera viewing angle was greater than 70° because the contribution to the measurement uncertainty due to directional emissivity becomes prohibitively large. Laminar computational solutions were generated for comparison using the NASA Langley Aerothermodynamic Upwind Relaxation Algorithm (LAURA)

[22, 23]. Details of the computations can be found in Reference [18]. The laminar heating distribution predicted by Lees' approximate solution to the boundary-layer equations [24] is also provided for comparison in Figure 23. The experimental heat transfer magnitudes agree well with the computational and theoretical predictions, although in general heating is lower than expected at the stagnation point and higher than expected at the shoulder. There is some uncertainty in the comparison related to the freestream conditions and normalization, but the relatively low heating at the stagnation point indicates a systematic bias likely introduced by either the material thermal properties or surface emissivity.

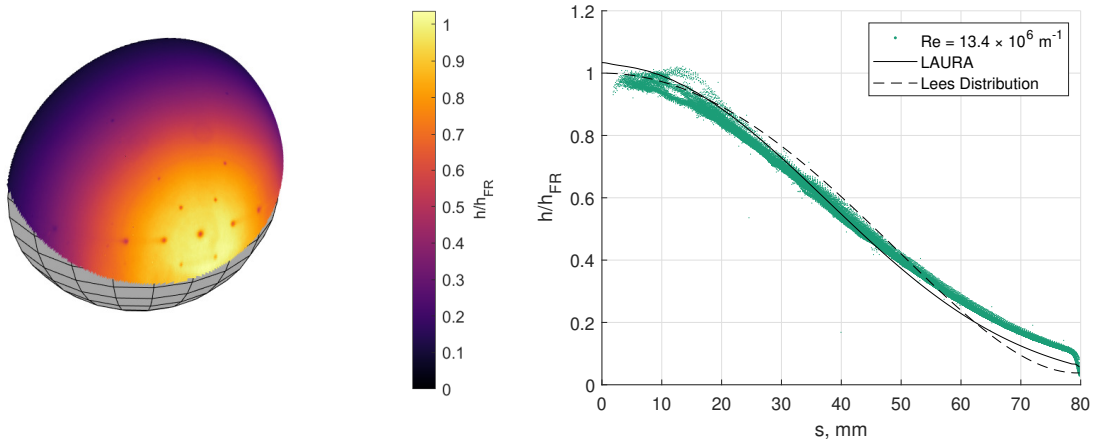

(a) Global normalized heat transfer coefficient **(b) Mapped heating**

Fig. 23 Normalized heat transfer coefficient for the PEEK model at Re = 13.4×10^6 m^{-1} ($\varepsilon_n = 0.93$).

There is also a noticeable variation of the heating in Figure 23 within approximately 20 mm of the stagnation point. Closer inspection of the IR imagery revealed similar variation in the measured counts near the stagnation point, as shown in Figure 24. This variation could not have been introduced by any of the surface temperature corrections and therefore must be an inherent property of the model surface. After the test was completed, the surface was scanned using a Keyence optical profilometer and the resulting data are given in Figure 25. The optical scan may show some qualitative variation of the surface reflectivity, although this observation is subtle, and it is unclear how this variation in reflectance would extend to the LWIR bandwidth. The nominal sphere surface was subtracted from the measured surface

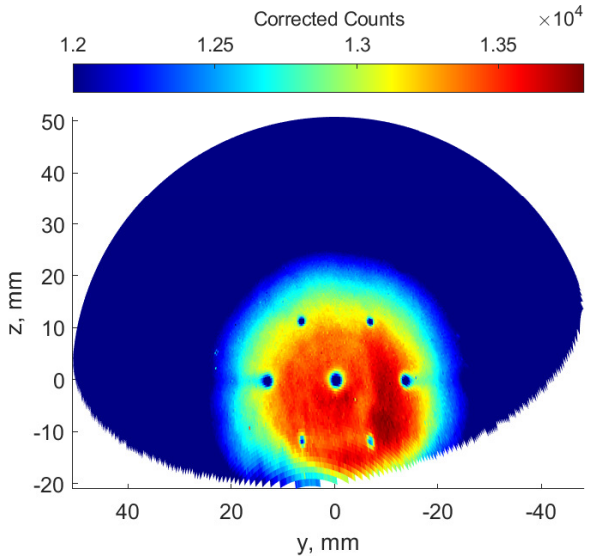

Fig. 24 Variation of the image counts observed near the stagnation point of the PEEK hemisphere.

profile to highlight local deviations from the theoretical surface. In the region surrounding the stagnation point, the surface was measured to be approximately 30 µm lower than expected. This is likely an artifact of the model fabrication or possibly from the installation of the stagnation point temperature gauge. There is a less likely possibility that this is damage to the model due to a combination of thermal cycling and particle impacts. However, particle impacts should be fairly minimal for the filtered freestream air and the surface temperature was only briefly observed to exceed the glass transition temperature. Regardless of the cause, the spread in the observed stagnation point heating is likely caused by some local variation of the model emissivity.

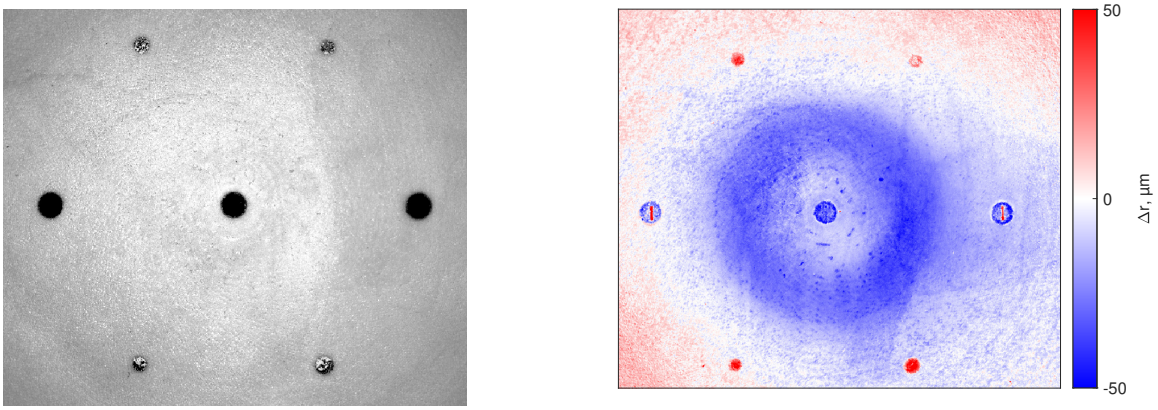

(a) Optical Scan **(b) Relative height**

Fig. 25 Keyence scans of the PEEK model stagnation point.

Values of the normalized heat transfer coefficient along one arc of the PEEK hemisphere are plotted in Figure 26 to demonstrate invariance of the heating with freestream unit Reynolds number. The Reynolds number collapse is remarkable and the extracted heating distributions are nearly indiscernible from each other. As was previously noted, the stagnation point heating for all freestream conditions is approximately 7-8% lower than that predicted by theory and

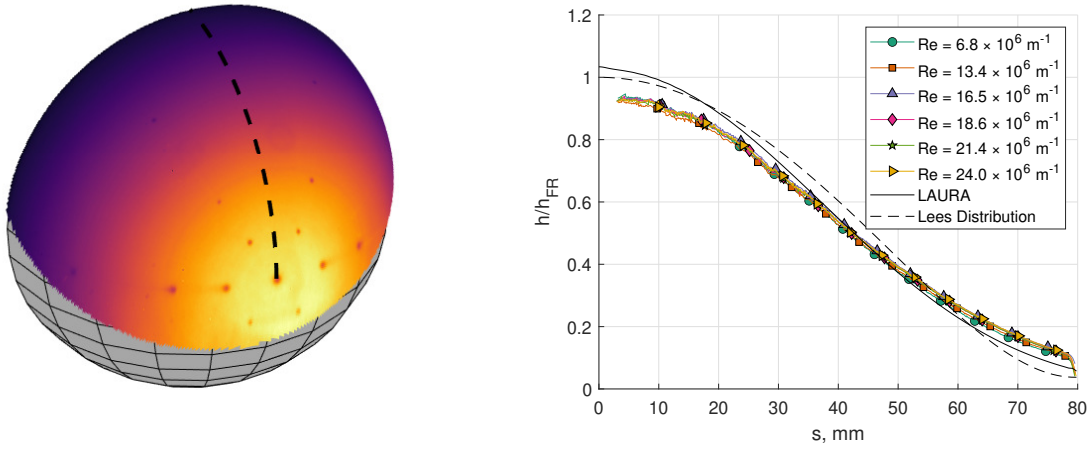

(a) Global heating and profile location **(b) Extracted heating profiles**

Fig. 26 Reynolds number collapse of the normalized heat transfer coefficient for the Re = 13.4×10^6 m^{-1} case. (ε_n = 0.93)

computations. Similar heating profiles are plotted in Figure 27 for the fused silica ceramic and Rigid 10K models. The agreement with predictions is significantly worse for these two materials as compared to the PEEK model. In the case of Rigid 10K, this could easily be explained by poor characterization of both the material thermal properties and the surface emissivity. In the case of the fused silica ceramic, however, the thermal properties have been well characterized as part of the phosphor thermography test technique. This would suggest that the actual emissivity of the fused silica ceramic is much higher than the value assumed for the calculation of heat flux.

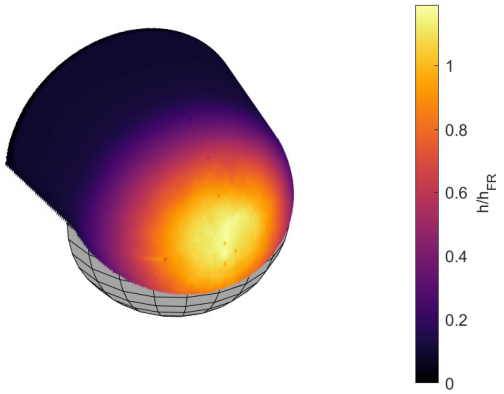

(a) Fused silica ceramic: surface heating

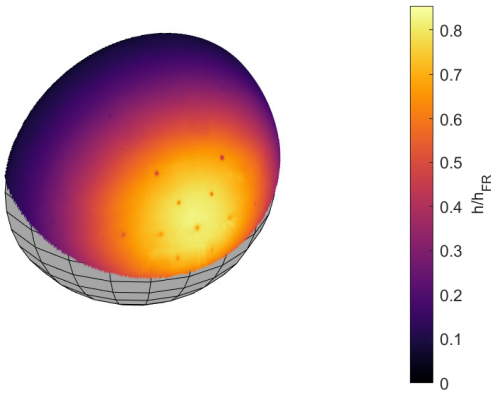

(b) Formlabs Rigid10K: surface heating

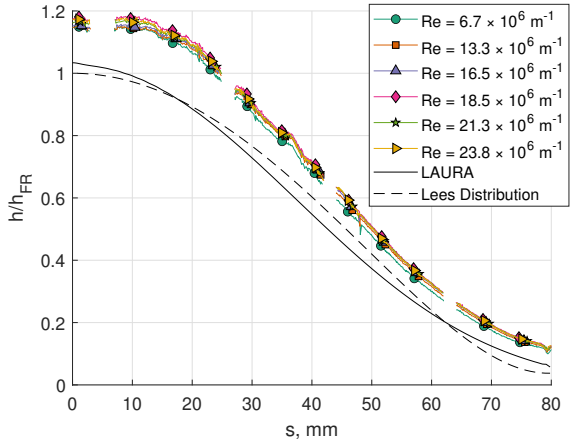

(c) Fused silica ceramic: heating profiles

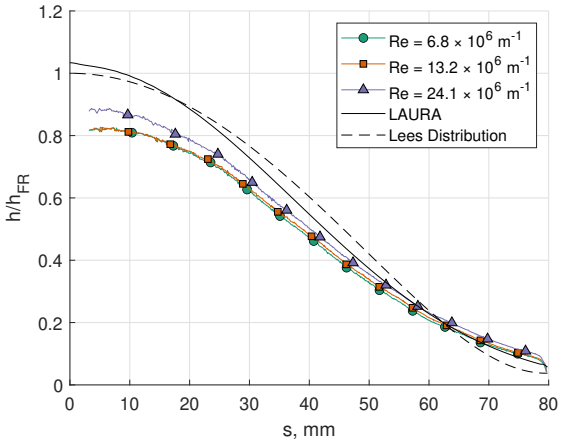

(d) Rigid 10K: heating profiles

Fig. 27 Heating results for the fused silica ceramic ($\varepsilon_n = 0.91$) and Formlabs Rigid 10K ($\varepsilon_n = 0.95$).

A complete estimate of the heat transfer measurement uncertainty is left for future work, but is expected to be dominated by uncertainties in the thermal properties and test article emissivity. Assuming typical uncertainties of 5% for both the specific heat capacity and thermal diffusivity, the heat transfer measurement uncertainty is expected to be approximately 7% due to thermal properties alone. To assess the sensitivity of the heating to emissivity, the normalized heat transfer coefficient was calculated for the PEEK model assuming normal emissivity values of 0.91, 0.93, and 0.95. These normal emissivities span the range of values that have been used in the literature for PEEK. Slices of the resulting heating are plotted in Figure 28. As expected, a lower emissivity yields a higher surface temperature and therefore a higher ΔT, yielding higher heat transfer magnitudes. This effect is more pronounced near the stagnation point where the surface temperatures are significantly higher. For a normal emissivity of 0.91, the heating agrees very well with the predictions from boundary-layer theory and is within 2% of the computational prediction. Given the sensitivity of the surface heating to the emissivity, better efforts will have to be made in the future to characterize the model materials. Even with perfect characterization, however, there is still a significant uncertainty in the emissivity for observations at

steep viewing angles. For cases where steep viewing angles cannot be avoided, or perhaps for cases where graybody assumptions breakdown, emissivity-correcting multispectral and hyperspectral variants of this IR technique should be evaluated [25]. Such efforts are the intended subject of future work.

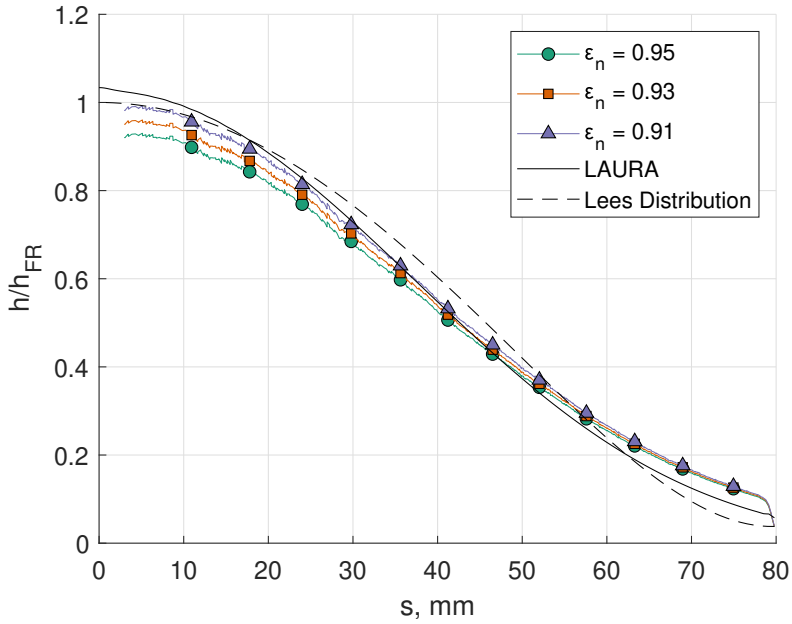

Fig. 28 Effect of normal emissivity on the surface heating. PEEK model at Re = 13.4×10^6 m^{-1}.

VI. Conclusion

An IR validation test campaign with 4-inch (101.6 mm) diameter hemisphere models was conducted in the NASA Langley Aerothermodynamic Laboratory 20-Inch Mach 6 Air Tunnel. The objective of this work was to assess the performance of a modern quantitative IR technique for measurement of global surface heat flux. Measurements were obtained for PEEK, fused silica ceramic, and Formlabs Rigid 10K hemispheres over a range of freestream Reynolds numbers. The raw IR images were corrected for transmission losses through the tunnel window, emissivity of the model, and reflection of the ambient environment and then converted to temperature via a radiometric calibration. Uncertainty of the surface temperature is estimated to be between 1 K and 4 K for camera viewing angles up to approximately 60°, which is comparable to a standard thermocouple uncertainty. The measured surface temperatures were reduced to heat flux using a finite-difference solution of the one-dimensional heat equation accounting for variable thermal properties. Results for the relatively well-characterized PEEK material show agreement to computations and theory within the expected uncertainty of the IR technique. An initial assessment demonstrates a strong dependence of the stagnation point heating on the surface emissivity, exacerbated by the high surface temperatures. Results for fused silica and Rigid 10K show poor agreement with predictions. Further investigation must be done to better characterize the thermal and emissive properties of prospective model materials.

Acknowledgments

This work was funded by the Hypersonics Technology Project (HTP) and the Aerosciences Evaluation and Test Capabilities (AETC) portfolio office. The authors would like to acknowledge Kevin Hollingsworth, Nick Shaw, Joe Rodriguez, Johnny Ellis, and Julia Musson for their help in the execution of this test.

References

[1] Merski, N. R., "Global Aeroheating Wind-Tunnel Measurements Using Improved Two-Color Phosphor Thermography Method," *Journal of Spacecraft and Rockets*, Vol. 36, No. 2, 1999, pp. 160–170. https://doi.org/10.2514/2.3446.

[2] Liu, T., Campbell, B., Burns, S., and Sullivan, J., "Temperature- and Pressure-Sensitive Luminescent Paints in Aerodynamics," *Applied Mechanics Reviews*, Vol. 50, No. 4, 1997, pp. 227–246.

[3] Astarita, T., and Carlomagno, G. M., *Infrared Thermography for Thermo-Fluid-Dynamics*, Springer, Berlin/Heidelberg, Germany, 2013.

[4] Zaccara, M., Edelman, J. B., and Cardone, G., "A General Procedure for Infrared Thermography Heat Transfer Measurements in Hypersonic Wind Tunnels," *International Journal of Heat and Mass Transfer*, Vol. 163, No. 120419, 2020, pp. 1–19.

[5] Estorf, M., "Ortsaufgelöste Bestimmung instationärer Wärmestromdichten in der Aerothermodynamik," Ph.D. thesis, Technische Universität Carolo Wilhemina zu Braunschweig, Braunschweig, Germany, 2008.

[6] Häberle, J., "Untersuchungen zum externen und internen Strömungsfeld eines Scramjet Triebwerkseinlaufs bei unterschiedlichen Betriebspunkten," Ph.D. thesis, Universität Stuttgart, Stuttgart, Germany, 2009.

[7] Turbeville, F. D., "Measurements of Transition Near the Corner Formed by a Highly-Swept Fin and a Cone at Mach 6," Ph.D. thesis, Purdue University, West Lafayette, Indiana, 2021.

[8] Wirth, J. M., and Bowersox, R. D. W., "Tunnel Environment Effects on the Single Fin-Cone at Mach 6," *AIAA Paper 2022-4137*, June 2022. https://doi.org/10.2514/6.2022-4137.

[9] Threadgill, J. A. S., Singh, A., Garcia, A. H. R., and Little, J. C., "Boundary Layer Separation on a Hollow-Cylinder/Flare at Mach 5," *AIAA Paper 2023-1246*, January 2023. https://doi.org/10.2514/6.2023-1246.

[10] Plummer, A. E., Padmanabhan, S., Singh, A., Threadgill, J. A. S., and Little, J. C., "Transitional Fin-Induced Shock Boundary Layer Interactions on a Hollow Cylinder Model at Mach 5," *AIAA Paper 2023-3700*, June 2023. https://doi.org/10.2514/6.2023-3700.

[11] Skora, A., and Craig, S. A., "Experimental Investigation of Transition on a 7-degree Cone at Mach 5," *AIAA Paper 2024-1517*, January 2024. https://doi.org/10.2514/6.2024-1517.

[12] Berger, K., Rufer, S., Hollingsworth, K., and Wright, S., "NASA Langley Aerothermodynamics Laboratory: Hypersonic Testing Capabilities," *AIAA Paper 2015-1337*, January 2015. https://doi.org/10.2514/6.2015-1337.

[13] Nguyen, N. M., Ruda, M. L., and Massa, L., "Nonlinear Estimators for Hypersonic Heat Flux Reconstruction," *Journal of Thermophysics and Heat Transfer*, 2024, p. Article in Advance. https://doi.org/10.2514/1.T6888.

[14] Bouguet, J. Y., "Camera Calibration Toolbox for Matlab," Computational Vision at the California Institute of Technology, 2022.

[15] Zhang, Z., "A Flexible Technique for Camera Calibration," *IEEE Transactions on Pattern Analysis and Machine Intelligence*, Vol. 22, No. 11, 2000, pp. 1330–1334.

[16] Heikkila, J., and Silven, O., "A Four-step Camera Calibration Procedure with Implicit Image Correction," *IEEE International Conference on Computer Vision and Pattern Recognition*, 1997.

[17] Baehr, H. D., and Stephan, K., *Heat and Mass Transfer*, Springer, Berlin/Heidelberg, Germany, 2011.

[18] Cheatwood, J. S., "The Patch Integral Method (PIM), a New Heat Transfer Analysis Tool for Hypersonic Wind Tunnel Facilities at NASA Langley," Master's thesis, Virginia Polytechnic Institute and State Univeristy, 2022.

[19] Mason, M. J., and Rufer, S. J., "Imaging for Hypersonic Experimental Aeroheating Testing (IHEAT) version 4.0: User Manual," Technical Memo TM-2018-220113, NASA Langley Research Center, November 2018.

[20] Kinsey, B., Skora, A., Ramesh, R., and Craig, S. A., "Quantitative Heat Transfer Measurements on a 3D Printed Hemisphere," *To be presented at AIAA Aviation Forum*, July 2024.

[21] Fay, J. A., and Riddell, F. R., "Theory of Stagnation Point Heat Transfer in Dissociated Air," *Journal of Aeronautical Sciences*, Vol. 25, No. 2, 1958, pp. 73–85.

[22] Gnoffo, P. A., "An Upwind-Biased, Point-Implicit Relaxation Algorithm for Viscous, Compressible Perfect-Gas Flows," Technical Paper 2953, NASA Langley Research Center, 1990.

[23] Thompson, K. B., Hollis, B. R., Johnston, C. O., Kleb, B., Lessard, V. R., and Mazaheri, A., "LAURA Users Manual: 5.6," Technical Memo TM-2020-220566, NASA Langley Research Center, February 2020.

[24] Lees, L., "Laminar Heat Transfer Over Blunt-Nosed Bodies at Hypersonic Flight Speeds," *Journal of Jet Propulsion*, Vol. 26, No. 4, 1956, pp. 259–269.

[25] Ianiro, A., and Cardone, G., "Measurement of Surface Temperature and Emissivity with Stereo Dual-Wavelength IR Thermography," *Journal of Modern Optics*, Vol. 57, No. 18, 2010.